The electron thermal structure in the dayside Martian ionosphere implied by the MGS radio occultation data

J. Cui[1], M. Galand[2], S. J. Zhang[3], E. Vigren[4], and H. Zou[5]

[1]Key Laboratory of Lunar and Deep Space Exploration, Chinese Academy of Sciences, Beijing, China, [2]Department of Physics, Imperial College, London, UK, [3]Shanghai Astronomical Observatory, Chinese Academy of Sciences, Shanghai, China, [4]Swedish Institute of Space Physics, Uppsala, Sweden, [5]School of Earth and Space Sciences, Beijing University, Beijing, China

Abstract We propose a revised Chapman model for the ionosphere of Mars by allowing for vertical variation of electron temperature. An approximate energy balance between solar EUV heating and CO_2 collisional cooling is applied in the dayside Martian ionosphere, analogous to the method recently proposed by Withers et al. (2014). The essence of the model is to separate the contributions of the neutral and electron thermal structures to the apparent width of the main ionospheric layer. Application of the model to the electron density profiles from the Mars Global Surveyor (MGS) radio occultation measurements reveals a clear trend of elevated electron temperature with increasing solar zenith angle (SZA). It also reveals that the characteristic length scale for the change of electron temperature with altitude decreases with increasing SZA. These observations may imply enhanced topside heat influx near the terminator, presumably an outcome of the solar wind interactions with the Martian upper atmosphere. Our analysis also reveals a tentative asymmetry in electron temperature between the northern and southern hemispheres, consistent with the scenario of elevated electron temperature within minimagnetospheres.

1. Motivation

A large number of electron density profiles in the Martian ionosphere have been obtained by radio occultation and/or radar sounding measurements made aboard several spacecraft [*Withers*, 2009, and references therein]. On the dayside, the Martian ionosphere contains a well-defined primary layer (M_2) and a low-altitude secondary layer (M_1) that have frequently drawn analogy to the terrestrial F_1 and E layers [*Rishbeth and Mendillo*, 2004]. The M_2 layer is mainly produced by solar EUV ionization and the M_1 layer by solar X-ray ionization along with impact ionization by photoelectrons and secondary electrons [e.g., *Martinis et al.*, 2003; *Fox and Yeager*, 2006; *Peter et al.*, 2014]. Extensive efforts have been devoted to understanding the density structures of both layers, showing that they are generally consistent with predictions of the idealized Chapman theory [e.g., *Morgan et al.*, 2008; *Fox and Yeager*, 2009; *Fox and Weber*, 2012].

Less well studied, however, is the electron thermal structure with the only available measurements made by the retarding potential analyzers (RPAs) aboard Viking Landers 1 and 2 (VL1 and VL2) at altitudes above the M_2 peak at low solar activity and at a solar zenith angle (SZA) of 44° [*Hanson and Mantas*, 1988]. Several numerical models have been developed so far to calculate the electron temperature profile in the Martian ionosphere, demonstrating that solar heating alone is insufficient to reproduce the Viking RPA data [e.g., *Chen et al.*, 1978; *Choi et al.*, 1998; *Matta et al.*, 2014]. Recently, *Withers et al.* [2014] proposed an innovative method to estimate electron temperature, which is analytic in nature and easily implemented. In this study, a revised Chapman model for the ionosphere of Mars is constructed based on their method. The model is applied to the Mars Global Surveyor (MGS) radio occultation data to investigate variations of the electron thermal structure near the M_2 peak.

2. The Revised Chapman Model

Chapman [1931a, 1931b] introduced a simplified description of the ionosphere produced by monochromatic photoionization of an atmosphere under hydrostatic equilibrium, which is expressed as

$$P_{em} \exp\left[1 - \frac{z - z_m}{H_n} - \exp\left(-\frac{z - z_m}{H_n} \right) \right] = \alpha N_e^2, \tag{1}$$

where the left-hand side (LHS) represents the electron production rate and the right-hand side (RHS) the electron loss rate. In equation (1), P_{em} is the peak electron production rate, z is the altitude, z_m is the altitude of peak electron production, H_n is the neutral density scale height assumed to be a constant, N_e is the electron number density, and α is the dissociative recombination coefficient of O_2^+, the most abundant molecular ion in the Martian ionosphere [*Hanson et al.*, 1977]. According to *Peverall et al.* [2001], $\alpha \approx \alpha_0 (T_{e0}/T_e)^{0.7}$ with T_e being the electron temperature and $\alpha_0 \approx 2.4 \times 10^{-7}$ cm^3 s^{-1} for a reference electron temperature of $T_{e0} \approx 300$ K. Accordingly, the electron density profile could be written as

$$N_e(z) = N_{em} \left[\frac{T_e(z)}{T_{em}} \right]^{0.35} \exp \left\{ \frac{1}{2} \left[1 - \frac{z - z_m}{H_n} - \exp \left(-\frac{z - z_m}{H_n} \right) \right] \right\}, \tag{2}$$

where N_{em} and T_{em} are the electron density and electron temperature at z_m. Equation (2) is different from the idealized Chapman function [*Chapman*, 1931a, 1931b] with the incorporation of the additional scaling factor, $(T_e/T_{em})^{0.35}$, which allows for an explicit vertical variation of electron temperature.

Following *Withers et al.* [2014], we then assume an ideal balance between solar EUV heating and CO_2 collisional cooling, formulated as

$$\epsilon \alpha_0 \left[\frac{T_{e0}}{T_e(z)} \right]^{0.7} N_e(z)^2 = K_e N_n(z) N_e(z) \frac{T_e(z) - T_n}{[T_e(z)]^{0.5}}, \tag{3}$$

where the LHS gives the heating rate and the RHS the cooling rate of thermal electrons (see equation (2) of *Withers et al.* [2014] with the electron production rate, P_e, replaced by their equation (1)). In equation (3), ϵ is the average thermal energy release per ionization event due to Coulomb collisions between photo-electrons (and their secondaries) and thermal electrons, and $K_e \approx 9.15 \times 10^{-14}$ eV cm^3 s^{-1} K$^{-1/2}$ is a constant characterizing the cooling rate that includes both vibrational and rotational excitations [see *Matta et al.*, 2014, equations (A12) and (A13)]. We derive ϵ based on a solar energy deposition model that has been successfully used to describe the suprathermal electron population in the sunlit ionospheres of Venus [*Cui et al.*, 2011] and Titan [*Galand et al.*, 2006]. The model, adapted to Mars and coupled with a fluid ionospheric model [*Matta et al.*, 2014], indicates that $\epsilon \approx 0.7$ eV near the M_2 peak at 12:00 local time on Mars and for low solar activity conditions. Under other conditions, the value of ϵ is likely different, but we argue in section 3.2 that the main conclusions of this paper are not influenced by the exact choice of ϵ. Also note that *Withers et al.* [2014] adopted a slightly lower ϵ value of ≈ 0.5 eV in their calculations.

In equation (3), the neutral temperature, T_n, is calculated from $T_n = M_a g H_n / k_B$, where M_a is the mean molecular mass, g is the acceleration of gravity, and k_B is the Boltzmann constant. We assume in this study constant values of M_a (≈ 44 amu) and g (≈ 345 cm s^{-2}). The former assumption could be tested by the neutral atmosphere composition model of *Nier and McElroy* [1977], from which we find that M_a is overestimated by less than 5% below 140 km. The background neutral density, N_n, in equation (3) can be obtained from

$$N_n(z) = \frac{1}{\sigma_a C_h H_n} \exp \left(-\frac{z - z_m}{H_n} \right), \tag{4}$$

where $\sigma_a \approx 3 \times 10^{-17}$ cm^2 is the average photoabsorption cross section of CO_2 at 20–90 nm and C_h is the Chapman grazing incidence function that depends on SZA. Here we have implicitly used the fact that the neutral density scale height is constant and that the altitude of peak electron production corresponds to where the optical depth for CO_2 photoabsorption is unity [*Fox et al.*, 2008].

Equation (2) is used to describe an observed electron density profile, with N_{em}, z_m, and H_n treated as independent parameters to be constrained by data-model comparison. The electron temperature profile, T_e, does not introduce any additional parameters because it can be numerically solved with equations (2) and (3) for a given combination of (N_{em}, z_m, and H_n).

The application of the revised Chapman model outlined above is subject to two major limitations. The first limitation is the choice of a constant thermal energy release per ionization event of 0.7 eV, which is overestimated well below the M_2 peak where the photoelectrons are overall more energetic leading to a larger proportion of energy spent in ionization [e.g., *Galand et al.*, 2009]. In practice, this sets the lower limit of model application to 10 km below the M_2 peak. The choice of a constant ϵ also prevents us from

investigating possible solar cycle variation of the electron temperature. The second limitation is the neglect of thermal conduction in local energy balance, which is clearly invalid at high altitudes [*Matta et al.*, 2014]. Following *Withers et al.* [2014], we place a fixed upper limit of model application at 140 km.

3. Trends of the Electron Thermal Structure

3.1. Overview

In this study, the revised Chapman model is applied to the MGS radio occultation data acquired over seven occultation seasons from December 1998 to June 2005 [*Tyler et al.*, 2001]. These data are directly available at the Geosciences Node of the NASA Planetary Data System (PDS) public archives (ftp://pds-geosciences.wustl.edu/mgs/mgs-m-rss-5-sdp-v1), in the form of vertical electron density profiles covering a SZA range of 70°–90°, a solar longitude range of 70°–227°, as well as two narrow latitude bands of 61°N–85°N and 65°S–69°S. Only the daily averaged electron density profiles are used in this study. Typically, 6–12 individual profiles were obtained within each day. These profiles are widely separated in longitude but with nearly identical latitude and SZA values. Accordingly, using the daily averaged profiles smears out any longitudinal variation [e.g., *Bougher et al.*, 2001], but the variations with SZA (section 3.2) and latitude (section 3.3) should be well retained.

As described in section 2, the portion of an electron density profile from 10 km below the M_2 peak to a fixed altitude of 140 km is included in the data-model comparison. We require arbitrarily that the width of the selected altitude range is at least 13 km, which is the typical scale over which the electron temperature increases by a factor of *e* (see below). This leads to the selection of 309 out of a total number of 670 daily averaged profiles used for investigating the electron thermal structure. These profiles cover the SZA range up to 85°. Profiles further approaching the terminator are not included, either because their peaks are at sufficiently high altitudes that the effects of thermal conduction can no longer be ignored or because the width of the selected altitude range is too narrow to constrain rigorously the model parameters.

The profiles of the neutral temperature, T_n, and the electron temperature, T_e, derived from the selected MGS data set reflect properly the situation of strong thermal coupling at the bottomside due to high neutral atmospheric densities and weak thermal coupling at the topside with large temperature differences [e.g., *Chen et al.*, 1978]. Based on our analysis, the altitude-independent neutral temperature, T_n, lies in the range of 120–210 K with a mean of 150 K, in broad agreement with the range inferred from previous measurements [e.g., *Nier and McElroy*, 1977; *Seiff and Kirk*, 1977; *Keating et al.*, 1998; *Withers*, 2006; *Forget et al.*, 2009; *McDunn et al.*, 2010; *Withers et al.*, 2011; *Chaufray et al.*, 2011]. The electron temperature at the peak of electron production, T_{em}, varies between 320 K and 570 K with a mean of 410 K, and the electron temperature scale height, L_e, varies between 9 km to 18 km with a mean of 13 km. Note that we do not assume a priori an exponential form for the vertical variation of electron temperature, T_e, but instead estimate L_e from a logarithmic linear fitting to each of the T_e profiles actually derived.

The above description is illustrated by the example in Figure 1, where we show with the solid circles the daily averaged electron density profile acquired by the MGS radio occultation experiments made on 19 January 2001. The thick dashed and solid lines give the idealized Chapman profile and the revised Chapman profile, respectively. It is evident that both models reproduce well the data over the altitude range included in the model fitting. However, the two models are to be distinguished in terms of how the underlying thermal structure is treated. In the figure inset, we present the temperature profiles for both neutrals and electrons, T_n and T_e, over the altitude range of interest. T_n is assumed to be a constant in both cases, with the value for idealized Chapman (dark dashed) being slightly higher than that for revised Chapman (dark solid). The solid circles give the electron temperature profile actually derived at the resolution of the raw electron density profile, whereas the light solid line gives the exponential fit with an electron temperature scale height of $L_e \approx 11.4$ km. We also note that both models fail to reproduce the observed electron densities at lower and higher altitudes. The disagreement at lower altitudes is clearly due to the neglect of the M_1 layer, whereas the disagreement at higher altitudes is due to the combination of several reasons, such as the breakdown of photochemical equilibrium and the importance of thermal conduction.

The electron temperature profiles cannot be directly compared to the VL1 RPA measurements which were made above 200 km [*Hanson and Mantas*, 1988]. Previous modeling efforts have included a heat influx at the top of the Martian ionosphere in order to reproduce the Viking RPA values [*Chen et al.*, 1978; *Choi et al.*, 1998; *Matta et al.*, 2014]. The corresponding electron temperature near the M_2 peak was found to be
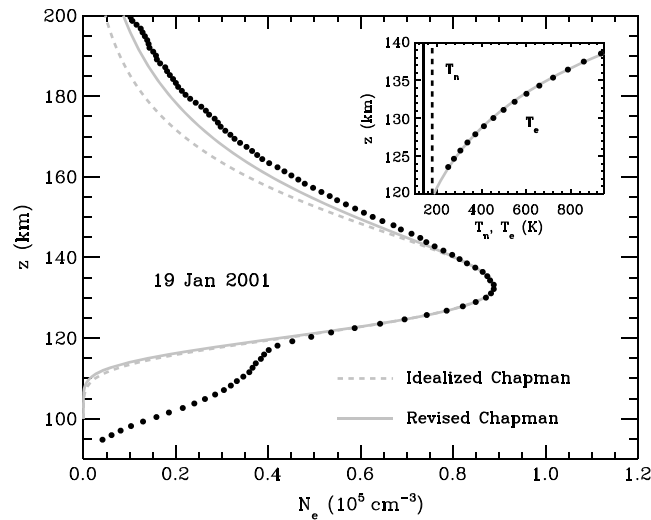
Figure 1. The electron density, N_e, as a function of altitude, z, acquired by the MGS radio occultation experiments made on 19 January 2001. The thick dashed and solid lines give the idealized Chapman profile and the revised Chapman profile, respectively. The figure inset shows the temperature profiles for both neutrals and electrons, T_n and T_e, over the altitude range of interest. T_n is assumed to be a constant in both cases, with the value for idealized Chapman (dark dashed) being slightly higher than that for revised Chapman (dark solid). The solid circles give the electron temperature profile actually derived at the resolution of the raw electron density profile, whereas the light solid line gives the exponential fit with an electron temperature scale height of $L_e \approx 11.4$ km.

≈ 200–300 K, which is somewhat lower than the T_{em} range found here. In addition, the nominal model of *Matta et al.* [2014] revealed a sharply increasing T_e from 137 K at 110 km to 1130 K at 160 km, implying an electron temperature scale height of ≈ 24 km. This is larger than the L_e values derived in the present study. We caution that previous calculations were made at SZA $\approx 44°$, whereas our results are appropriate for the near-terminator conditions. Therefore, the above distinctions in T_{em} and L_e may have important implications on the SZA variation of the electron thermal structure in the Martian ionosphere, which we examine below.
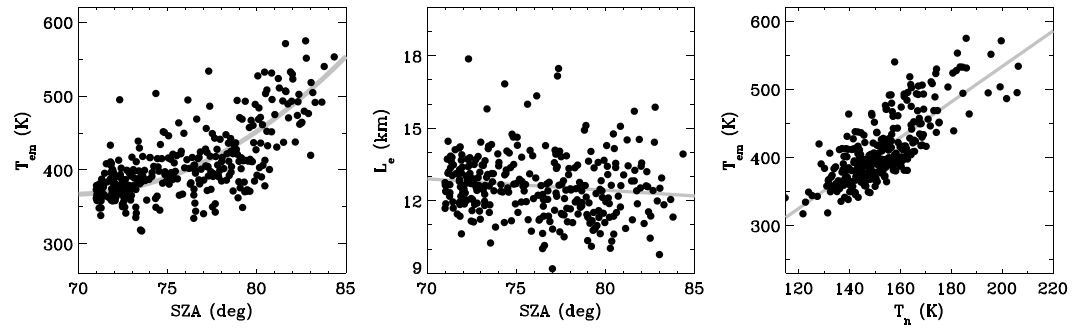
3.2. SZA Variation

The revised Chapman model fitting provides for each daily averaged electron density profile a set of best fit parameters including the altitude of peak electron production, z_m, the electron density at z_m, N_{em}, and the neutral density scale height, H_n.

The SZA variations of these parameters are shown by the dark circles in Figure 2, where the corresponding variations for idealized Chapman, z'_m, N'_{em}, and H'_n, are given by the light circles for comparison. The differences between the two sets of parameters are an important issue of this study and are discussed in details in section 4. Here we caution that at the face value, Figure 2 (middle) reveals a slight decrease in peak altitude with increasing SZA, in contrary to the expected behavior shown by numerous existing works [e.g., *Fox and Weber*, 2012, and references therein]. However, we remind that the revised Chapman model fitting is selectively applied to a portion of the observed electron density profiles for which the influence of thermal conduction is thought to be of minor importance (see section 2). This leads to the biased sampling that favors profiles peaking at relatively low altitudes. Indeed, the idealized Chapman model fitting to the
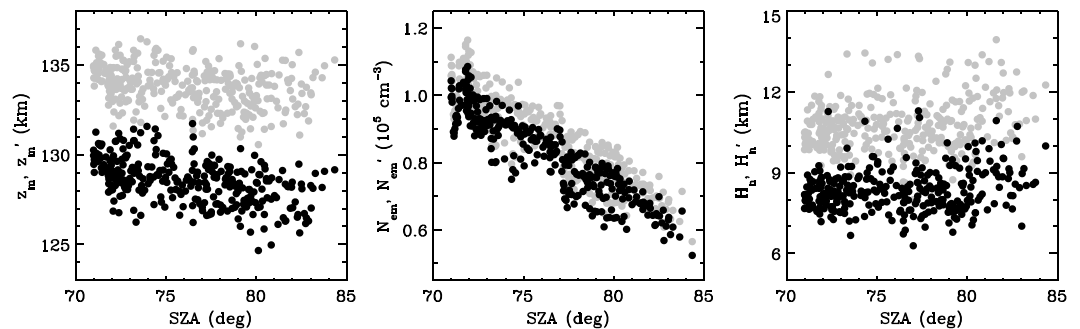
Figure 2. (left to right) The SZA variations of the altitude of peak electron production, z_m, the electron density at z_m, N_{em}, and the neutral scale height, H_n, all obtained from the revised Chapman model fitting to the MGS radio occultation data. Also shown in the figure are the SZA variations of similar parameters obtained by assuming idealized Chapman, denoted as z'_m, N'_{em}, and H'_n. The dark circles are for revised Chapman, and the light circles for idealized Chapman, respectively. A detailed comparison between the two sets of parameters is presented in section 4. We caution that the apparent decrease in peak altitude with increasing SZA, as shown in Figure 2 (middle), reflects biased sample selection rather than physical reality (see text for details).

Figure 3. (left to right) The SZA variations of the electron temperature at the altitude of peak electron production, T_{em}, as well as the electron temperature scale height, L_e, obtained from the revised Chapman model fitting to the MGS radio occultation data. Also shown is the relation between T_{em} and the neutral temperature, T_n, of which the latter is assumed to be a constant for each individual electron density profile. The thick solid line in each panel gives the best fit relation, either second-order polynomial or linear (see text for details).

entire data set does confirm the expected behavior of a general increase in peak altitude with increasing SZA (not shown in Figure 2).

An additional parameter derived from the revised Chapman model fitting is the electron temperature at z_m, T_{em}, which cannot be obtained from idealized Chapman. The SZA variation of this parameter is shown in Figure 3 (left), revealing that on average T_{em} increases from ≈ 370 K at SZA $= 70°$ to ≈ 550 K at SZA$=85°$. The linear Pearson correlation coefficient between SZA and T_{em} is ≈ 0.68, and the correlation could be reasonably described by

$$T_{em} \approx 4190 - 110 \times \text{SZA} + 0.788 \times \text{SZA}^2, \tag{5}$$

where T_{em} is given in kelvin and SZA in degree. The electron temperature scale height, L_e, also shows a SZA trend as illustrated in Figure 3 (middle), though much weaker with a linear Pearson correlation coefficient of ≈ -0.13 and a best fit linear relation of

$$L_e \approx 16.2 - 0.047 \times \text{SZA}, \tag{6}$$

where L_e is given in kilometer and SZA in degree. Specifically, L_e decreases slightly from ≈ 13 km at SZA$=70°$ to ≈ 12 km at SZA$=85°$. We also show the relation between T_n and T_{em} in Figure 3 (right), with the clear correlation consistent with the expected strong thermal coupling between the neutral upper atmosphere and ionosphere [e.g., *Matta et al.*, 2014]. The corresponding Pearson correlation coefficient is ≈ 0.77, and the linear fit is given by

$$T_{em} \approx 2.64 \times T_n, \tag{7}$$

where both T_n and T_{em} are given in kelvin.

The typical uncertainty in electron density near the M_2 peak is 10% [e.g., *Breus et al.*, 2004]. This leads to an uncertainty in T_{em} of $\approx 8\%$ according to equation (3), which is not large enough to influence the observed increase of $\approx 50\%$ from SZA $= 70°$ to $85°$. Standard χ^2 analysis confirms our expectation that the uncertainties in electron temperature related to uncertainties in electron density are of minor importance [*Press et al.*, 1992]. Within the context of this study, main sources of uncertainty likely come from the choices of some model parameters as well as the model assumption of negligible thermal conduction detailed as follows.

First, we note that the derived electron temperatures depend on the choices of the average thermal energy release per ionization event, ϵ, and the constant characterizing the cooling rate, K_e. According to equation (3), it is really the ratio, ϵ/K_e, that matters. The effect of a varying ϵ/K_e is to shift the SZA-T_{em} and SZA-L_e relations in Figure 3 either upward or downward, whereas the overall trends remain nearly unaffected. For example, keeping K_e unchanged but decreasing ϵ to 0.5 eV (the same value as adopted in *Withers et al.* [2014]) reduces T_{em} to ≈ 320 K at SZA$=70°$ and ≈ 440 K at SZA$=85°$ with a linear Pearson correlation coefficient of ≈ 0.64.

Second, another potentially important uncertainty comes from the effect of thermal conduction, though we have limited model application to altitudes below 140 km. Qualitatively, such an effect reduces both the local electron temperature and electron temperature gradient, especially at large SZA where it becomes more effective due to the elevation of the M_2 peak. To exclude this possibility, we examine further the SZA variation of the electron temperature at a fixed altitude of 125 km. This is a sufficiently low altitude where the contribution of thermal conduction to the local energy budget is no more than $\approx 5\%$ [see *Matta et al.*, 2014, Figure 6]. Our analysis shows that T_e now increases from ≈ 270 K at SZA = 70° to ≈ 450 K at SZA = 85°, similar to the trend in Figure 3. We also mention above that to avoid the influence of thermal conduction, the sample used in this study preferentially selects profiles that peak at relatively low altitudes (see Figure 2, middle). This means that the actual SZA variation of T_{em}, when corrected for such a sampling bias, might be even stronger as electron temperature increases with increasing altitude (see Figure 1 inset).

Based on the modeling results of *Matta et al.* [2014], the electron temperature at a fixed SZA increases sharply with increasing altitude, whereas the electron temperature at a fixed altitude decreases with increasing SZA. The combined effect is a gentle increase in T_{em} over the SZA range shown in Figure 3. Specifically, the calculations of *Matta et al.* [2014] reveal that at a fixed altitude of 125 km, electron temperature decreases from ≈ 246 K at SZA = 70° to ≈ 188 K at SZA = 85°, whereas at the peak of electron production, T_{em} increases modestly from ≈ 335 K to ≈ 390 K over the same SZA range. Therefore, it is clear that the modeling result of *Matta et al.* [2014] is in disagreement with our findings. We emphasize that their results come from a coupled fluid and kinetic model of the Martian ionosphere purely driven by solar radiation, whereas ours are directly constrained by the observations with the aid of the condition for local energy balance. Clearly, the solar-driven scenario is incapable of reproducing the data.

Despite a similar approach used here and used by *Withers et al.* [2014], the SZA variation of the electron temperature obtained by the latter is similar to that of *Matta et al.* [2014], thus different from ours. However, we caution that the result of *Withers et al.* [2014] ought to be regarded as a prediction under representative physical conditions (e.g., a constant neutral temperature of 181 K and a constant solar ionizing flux of 10^{10} cm^{-2} s^{-1} were assumed), whereas our result is directly constrained by the data. One key argument made by *Withers et al.* [2014] is that the scaling of electron density at the peak with C_h to the power of -0.5 is ensured by the insignificant SZA variation of electron temperature at the peak. For comparison, the strong SZA variation in T_{em} in our case leads to the observed variation in N_{em} (see Figure 2) that scales with C_h to the power of -0.55. Such a difference in the SZA variation of N_{em} is acceptable since existing works reveal a range of possible power index from ≈ -0.41 [e.g., *Fox and Yeager*, 2006] to ≈ -0.57 [e.g., *Hantsch and Bauer* 1990].

It is known from existing calculations that an ad hoc heat influx from the top of the Martian atmosphere has to be invoked to match the Viking RPA measurements [e.g., *Chen et al.*, 1978; *Choi et al.*, 1998; *Matta et al.*, 2014]. Accordingly, the SZA trend of electron temperature revealed in Figure 3 (left) may imply an enhanced heat influx at large SZA. The calculations of *Choi et al.* [1998] further indicate that the electron temperature scale height tends to decrease with increasing levels of topside heat influx (see their Figure 2), which is consistent with the trend implied by Figure 3 (middle). If the above arguments are true, we speculate that the solar wind (SW) interactions with the Martian upper atmosphere play a crucial role since the ambient magnetic field lines at the latitudes of interest tend to be more open and vertical with increasing SZA, which facilitates access of precipitating SW electrons [e.g., *Brain et al.*, 2010, and references therein]. Such a conjecture remains to be verified by rigorous calculations that treat precipitating SW electrons as the primary source of topside heat influx and also incorporate large-scale variations in the ambient magnetic field configuration. Similar calculations have been made at the nightside of the Martian ionosphere but only focused on electron impact ionization rate [e.g., *Fillingim et al.*, 2007; *Lillis et al.*, 2009, 2011].

3.3. Hemispheric Asymmetry

The electron thermal structure in the Martian ionosphere is likely to be modified by the presence of strong crustal magnetic anomalies, which may produce isolated minimagnetospheres, trap photoelectrons, and enhance solar EUV heating via Coulomb collisions between photoelectrons (and their secondaries) and thermal electrons. Such a process is manifested as increased electron densities that coincide with the locations of strong crustal magnetic fields [e.g., *Krymskii et al.*, 2003; *Duru et al.*, 2006]. It is well known that on Mars, the crustal magnetic fields tend to be stronger at the southern hemisphere than the northern

hemisphere [e.g., *Acuña et al.*, 1998, 1999]. This motivates us to examine possible hemispheric asymmetry in the derived electron thermal structure.

Of the 307 daily averaged electron density profiles studied here, only 13 lie at the southern hemisphere, with a median electron temperature of ≈ 490 K at the altitude of peak electron production, z_m, ≈ 810 K at the altitude of peak electron density, z'_m, or ≈ 440 K at a reference altitude of 125 km. At the northern hemisphere, the respective median temperatures are ≈ 400 K at z_m, ≈ 600 K at z'_m, or ≈ 290 K at 125 km, about 20%–35% lower than the southern hemisphere values. We note that the two hemispheres are not identically sampled in SZA, with four profiles (30%) from the southern hemisphere obtained at SZA $= 78°$–$80°$ and 9 (70%) at SZA $= 80°$–$85°$. To remove the biased sampling, we also calculate the electron temperatures at the northern hemisphere weighted by the above sampling rate, which are ≈ 460 K at z_m, ≈ 730 K at z'_m, and ≈ 340 K at 125 km, now lower than the mean southern hemisphere values by about 10%–25%.

For comparison, *Breus et al.* [2004] estimated the mean electron temperature at the southern hemisphere to be higher than the mean northern hemisphere value by 50%–60%, referring to the altitude of peak electron density, z'_m, and uncorrected for the hemispheric difference in SZA sampling. However, we note that a constant energy release per ionization event of 0.7 eV is used throughout this study (see section 2), which means that any influence of the solar cycle variation on electron thermal structure has been ignored. In contrast, such an influence was taken into account by *Breus et al.* [2004], who noticed that the solar ionizing flux for measurements made at the southern hemisphere was lower than that for northern hemisphere measurements. Bearing such a difference in mind, we expect the hemispheric difference in electron temperature reported here to be underestimated.

Clearly, both our analysis and that of *Breus et al.* [2004] reveal a tentative hemispheric asymmetry consistent with the expectation of elevated electron temperatures within minimagnetospheres [e.g., *Krymskii et al.*, 2003], despite that the two works derive information on electron temperature with remarkably different approaches. In *Breus et al.* [2004], the idealized Chapman model was assumed, with electron temperature inferred from a comparison in electron density between the two hemispheres. Specifically, they attributed the electron density difference to difference in O_2^+ dissociative recombination coefficient, which is in turn indicative of difference in electron temperature. In contrast, the idealized Chapman model is not assumed in this study, with electron temperature inferred directly from the local energy budget at altitudes where the effect of thermal conduction is likely of minor importance. Clearly, absolute values of electron temperature can be obtained here, whereas only relative ratios are available with the *Breus et al.* [2004] approach.

4. Discussions

It is instructive to compare the best fit values of peak electron density, peak altitude, and neutral density scale height, N_{em}, z_m and H_n, from the revised Chapman model with the values from the idealized Chapman model, denoted as N'_{em}, z'_m, and H'_n (see Figure 2). The latter are derived following the procedure of *Withers and Mendillo* [2005] based on the Taylor expansion of the logarithmic electron density near the M_2 peak (see their equation (5)). The difference between z'_m and z_m essentially reflects the difference in altitude between peak electron density and peak electron production. Specifically, we find that z'_m is higher than z_m by ≈ 4.6 km on average, generally consistent with the prediction of *Fox and Yeager* [2006]. We note that their result was obtained with model electron density profiles in the dayside Martian ionosphere, whereas ours is based on realistic data. The difference between z'_m and z_m is clearly attributed to a positive electron temperature gradient. This naturally leads to a difference between N_{em} and N'_{em} with $\left(N'_{em} - N_{em}\right) / N_{em} \approx 5.5\%$ on average based on our analysis.

Of particular interest to this study is the difference in neutral density scale height between the two models, H_n and H'_n, as shown in Figure 2 (right). The figure reveals that H'_n tends to be systematically larger than H_n with $H'_n - H_n \approx 2.2$ km on average. Such a difference is also related to the electron temperature gradient which has the effect of broadening the electron density distribution [e.g., *Fox and Yeager*, 2006]. This means that for the idealized Chapman model, the observed width in electron density is entirely related to the neutral density scale height, whereas for the revised Chapman model, part of the width is attributed to the electron temperature gradient. Such a feature highlights the coupling between the underlying neutral and electron thermal structures. At the face value, an observed electron density profile could be reproduced by either the combination of a cooler neutral atmosphere and a steeper electron temperature increase or the

combination of a hotter neutral atmosphere and a gentler electron temperature increase. It is the condition for local energy balance (see equation (3)) that breaks the coupling and picks out a unique solution among all possibilities. This is the whole essence of the revised Chapman model proposed here.

Previous analyses of the radio occultation and radar sounding data of the Martian ionosphere have indicated a trend of increasing width of the M_2 layer with increasing SZA [e.g., *Němec et al.*, 2011; *Sánchez-Cano et al.*, 2013]. Within the framework of the idealized Chapman theory, this is fully accounted for by an elevated neutral density scale height or neutral temperature near the terminator, for which no viable mechanism exists. In this study, however, the SZA variation of the layer width is, at least partly, attributed to the SZA variation of the electron thermal structure. The modest increase in neutral temperature as approaching the terminator (see Figure 2 (right)) is a natural result of enhanced neutral heating via collisions with photoelectrons and/or secondary electrons there.

5. Concluding Remarks

Numerous previous works show that the variations of the Martian ionosphere are in good agreement with predictions of the idealized Chapman model [*Withers*, 2009, and references therein], despite that such a model makes an unrealistic assumption of a constant electron temperature at ionospheric altitudes. The present work is based on a revised Chapman model assuming an approximate energy balance between solar EUV heating and CO_2 collisional cooling, as recently proposed by *Withers et al.* [2014]. The model is analytic in nature and easily implemented but only applicable to the electron distribution near the M_2 peak due to the neglect of thermal conduction and the assumption of a constant thermal energy release of 0.7 eV per ionization event. With the revised Chapman model, the apparent width of the M_2 layer is determined by both the neutral density scale height and the electron temperature scale height, in contrary to the idealized Chapman case with the layer width fully determined by the former. The above fact highlights the coupling between the neutral and electron thermal structures in reproducing an observed electron density profile. It is the condition for local energy balance that picks out a unique solution among all possibilities.

Implementation of the revised Chapman model to the MGS radio occultation data reveals a clear trend of elevated electron temperature and a weak trend of reduced electron temperature scale height near the M_2 peak, both with increasing SZA. These results are in conflict with predictions of purely solar-driven models [*Matta et al.*, 2014]. We speculate that they are indicative of enhanced topside heat influx near the terminator, presumably related to the SW interactions with the Martian upper atmosphere modulated by the ambient magnetic field configuration. We also find a tentative asymmetry in electron temperature between the northern and southern hemispheres, which is consistent with the scenario of elevated electron temperature within minimagnetospheres.

References

Acuña, M. H., et al. (1998), Magnetic field and plasma observations at Mars: Initial results of the Mars Global Surveyor mission, *Science*, *279*, 1676–1680, doi:10.1126/science.279.5357.1676.

Acuña, M. H., et al. (1999), Global distribution of crustal magnetization discovered by the Mars Global Surveyor MAG/ER experiment, *Science*, *284*, 790–793, doi:10.1126/science.284.5415.790.

Bougher, S. W., S. Engel, D. P. Hinson, and J. M. Forbes (2001), Mars Global Surveyor radio science electron density profiles: Neutral atmosphere implications, *Geophys. Res. Lett.*, *28*, 3091–3094, doi:10.1029/2001GL012884.

Brain, D., et al. (2010), A comparison of global models for the solar wind interaction with Mars, *Icarus*, *206*, 139–151, doi:10.1016/j.icarus.2009.06.030.

Breus, T. K., A. M. Krymskii, D. H. Crider, N. F. Ness, D. Hinson, and K. K. Barashyan (2004), Effect of the solar radiation in the topside atmosphere/ionosphere of Mars: Mars Global Surveyor observations, *J. Geophys. Res.*, *109*, A09310, doi:10.1029/2004JA010431.

Chapman, S. (1931a), The absorption and dissociative or ionizing effect of monochromatic radiation in an atmosphere on a rotating Earth, *Proc. Phys. Soc.*, *43*, 26–45.

Chapman, S. (1931b), The absorption and dissociative or ionizing effect of monochromatic radiation in an atmosphere on a rotating Earth—Part II. Grazing incidence, *Proc. Phys. Soc.*, *43*, 483–501.

Chaufray, J.-Y., et al. (2011), The density of the upper martian atmosphere measured by Lyman-α absorption with Mars Express SPICAM, *Icarus*, *215*, 522–525, doi:10.1016/j.icarus.2011.07.025.

Chen, R. H., T. E. Cravens, and A. F. Nagy (1978), The Martian ionosphere in light of the Viking observations, *J. Geophys. Res.*, *83*, 3871–3876, doi:10.1029/JA083iA08p03871.

Choi, Y. W., J. Kim, K. W. Min, A. F. Nagy, and K. I. Oyama (1998), Effect of the magnetic field on the energetics of Mars ionosphere, *Geophys Res. Lett.*, *25*, 2753–2756, doi:10.1029/98GL51839.

Cui, J., M. Galand, A. J. Coates, T. L. Zhang, and I. C. F. Müller-Wodarg (2011), Suprathermal electron spectra in the Venus ionosphere, *J. Geophys. Res.*, *116*, A04321, doi:10.1029/2010JA016153.

Duru, F., D. A. Gurnett, T. F. Averkamp, D. L. Kirchner, R. L. Huff, A. M. Persoon, J. J. Plaut, and G. Picardi (2006), Magnetically controlled structures in the ionosphere of Mars, *J. Geophys. Res.*, *111*, A12204, doi:10.1029/2006JA011975.

Fillingim, M. O., L. M. Peticolas, R. J. Lillis, D. A. Brain, J. S. Halekas, D. L. Mitchell, R. P. Lin, D. Lummerzheim, S. W. Bougher, and D. L. Kirchner (2007), Model calculations of electron precipitation induced ionization patches on the nightside of Mars, *Geophys. Res. Lett.*, *34*, L12101, doi:10.1029/2007GL029986.

Forget, F., F. Montmessin, J.-L. Bertaux, F. González-Galindo, S. Lebonnois, E. Quémerais, A. Reberac, E. Dimarells, and M. A. López-Valverde (2009), Density and temperatures of the upper Martian atmosphere measured by stellar occultations with Mars Express SPICAM, *J. Geophys. Res.*, *114*, E01004, doi:10.1029/2008JE003086.

Fox, J. L., and K. E. Yeager (2006), Morphology of the near-terminator Martian ionosphere: A comparison of models and data, *J. Geophys. Res.*, *111*, A10309, doi:10.1029/2006JA011697.

Fox, J. L., and K. E. Yeager (2009), MGS electron density profiles: Analysis of the peak magnitudes, *Icarus*, *200*, 468–479, doi:10.1016/j.icarus.2008.12.002.

Fox, J. L., and A. J. Weber (2012), MGS electron density profiles: Analysis and modeling of peak altitudes, *Icarus*, *221*, 1002–1019, doi:10.1016/j.icarus.2012.10.002.

Fox, J. L., M. I. Galand, and R. E. Johnson (2008), Energy deposition in planetary atmospheres by charged particles and solar photons, *Space Sci. Rev.*, *139*, 3–62, doi:10.1007/s11214-008-9403-7.

Galand, M., R. V. Yelle, A. J. Coates, H. Backes, and J.-E. Wahlund (2006), Electron temperature of Titan's sunlit ionosphere, *Geophys. Res. Lett.*, *33*, L21101, doi:10.1029/2006GL027488.

Galand, M., L. Moore, B. Charnay, I. Mueller-Wodarg, and M. Mendillo (2009), Solar primary and secondary ionization at Saturn, *J. Geophys. Res.*, *114*, A06313, doi:10.1029/2008JA013981.

Hanson, W. B., and G. P. Mantas (1988), Viking electron temperature measurements—Evidence for a magnetic field in the Martian ionosphere, *J. Geophys. Res.*, *93*, 7538–7544, doi:10.1029/JA093iA07p07538.

Hanson, W. B., S. Sanatani, and D. R. Zuccaro (1977), The Martian ionosphere as observed by the Viking retarding potential analyzers, *J. Geophys. Res.*, *82*, 4351–4363, doi:10.1029/JS082i028p04351.

Hantsch, M. H., and S. J. Bauer (1990), Solar control of the Mars ionosphere, *Planet. Space Sci.*, *38*, 539–542, doi:10.1016/0032-0633(90)90146-H.

Keating, G. M., et al. (1998), The structure of the upper atmosphere of Mars: In situ accelerometer measurements from Mars Global Surveyor, *Science*, *279*, 1672–1676, doi:10.1126/science.279.5357.1672.

Krymskii, A. M., T. K. Breus, N. F. Ness, D. P. Hinson, and D. I. Bojkov (2003), Effect of crustal magnetic fields on the near terminator ionosphere at Mars: Comparison of in situ magnetic field measurements with the data of radio science experiments on board Mars Global Surveyor, *J. Geophys. Res.*, *108*(A12), 1431, doi:10.1029/2002JA009662.

Lillis, R. J., M. O. Fillingim, L. M. Peticolas, D. A. Brain, R. P. Lin, and S. W. Bougher (2009), Nightside ionosphere of Mars: Modeling the effects of crustal magnetic fields and electron pitch angle distributions on electron impact ionization, *J. Geophys. Res.*, *114*, E11009, doi:10.1029/2009JE003379.

Lillis, R. J., M. O. Fillingim, and D. A. Brain (2011), Three-dimensional structure of the Martian nightside ionosphere: Predicted rates of impact ionization from Mars Global Surveyor magnetometer and electron reflectometer measurements of precipitating electrons, *J. Geophys. Res.*, *116*, A12317, doi:10.1029/2011JA016982.

Martinis, C. R., J. K. Wilson, and M. J. Mendillo (2003), Modeling day-to-day ionospheric variability on Mars, *J. Geophys. Res.*, *108*(A10), 1383, doi:10.1029/2003JA009973.

Matta, M., M. Galand, L. Moore, M. Mendillo, and P. Withers (2014), Numerical simulations of ion and electron temperatures in the ionosphere of Mars: Multiple ions and diurnal variations, *Icarus*, *227*, 78–88, doi:10.1016/j.icarus.2013.09.006.

McDunn, T., S. W. Bougher, J. Murphy, M. D. Smith, F. Forget, J.-L. Bertaux, and F. Montmessin (2010), Simulating the density and thermal structure of the middle atmosphere (80-130 km) of Mars using the MGCM-MTGCM: A comparison with MEX/SPICAM observations, *Icarus*, *206*, 5–17, doi:10.1016/j.icarus.2009.06.034.

Morgan, D. D., D. A. Gurnett, D. L. Kirchner, J. L. Fox, E. Nielsen, and J. J. Plaut (2008), Variation of the Martian ionospheric electron density from Mars Express radar soundings, *J. Geophys. Res.*, *113*, A09303, doi:10.1029/2008JA013313.

Němec, F., D. D. Morgan, D. A. Gurnett, F. Duru, and V. Truhlík (2011), Dayside ionosphere of Mars: Empirical model based on data from the MARSIS instrument, *J. Geophys. Res.*, *116*, E07003, doi:10.1029/2010JE003789.

Nier, A. O., and M. B. McElroy (1977), Composition and structure of Mars' upper atmosphere—Results from the neutral mass spectrometers on Viking 1 and 2, *J. Geophys. Res.*, *82*, 4341–4349, doi:10.1029/JS082i028p04341.

Peter, K., et al. (2014), The dayside ionospheres of Mars and Venus: Comparing a one-dimensional photochemical model with MaRS (Mars Express) and VeRa (Venus Express) observations, *Icarus*, *233*, 66–82, doi:10.1016/j.icarus.2014.01.028.

Peverall, R., et al. (2001), Dissociative recombination and excitation of O_2^+: Cross sections, product yields and implications for studies of ionospheric airglows, *J. Chem. Phys.*, *114*, 6679–6689, doi:10.1063/1.1349079.

Press, W. H., et al. (1992), *Numerical Recipes in C*, pp. 656–699, 2nd ed., Cambridge Univ. Press, Cambridge, U. K.

Rishbeth, H., and M. Mendillo (2004), Ionospheric layers of Mars and Earth, *Planet. Space Sci.*, *52*, 849–852, doi:10.1016/j.pss.2004.02.007.

Sánchez-Cano, B., S. M. Radicella, M. Herraiz, O. Witasse, and G. Rodríguez-Caderot (2013), NeMars: An empirical model of the Martian dayside ionosphere based on Mars Express MARSIS data, *Icarus*, *225*, 236–247, doi:10.1016/j.icarus.2013.03.021.

Seiff, A., and D. B. Kirk (1977), Structure of the atmosphere of Mars in summer at mid-latitudes, *J. Geophys. Res.*, *82*, 4364–4378, doi:10.1029/JS082i028p04364.

Tyler, G. L., G. Balmino, D. P. Hinson, W. L. Sjogren, D. E. Smith, R. A. Simpson, S. W. Asmar, P. Priest, and J. D. Twicken (2001), Radio science observations with Mars Global Surveyor: Orbit insertion through one Mars year in mapping orbit, *J. Geophys. Res.*, *106*, 23,327–23,348, doi:10.1029/2000JE001348.

Withers, P. (2006), Mars Global Surveyor and Mars Odyssey Accelerometer observations of the Martian upper atmosphere during aerobraking, *Geophys. Res. Lett.*, *33*, L02201, doi:10.1029/2005GL024447.

Withers, P. (2009), A review of observed variability in the dayside ionosphere of Mars, *Adv. Space Res.*, *44*, 277–307, doi:10.1016/j.asr.2009.04.027.

Withers, P., and M. Mendillo (2005), Response of peak electron densities in the martian ionosphere to day-to-day changes in solar flux due to solar rotation, *Planet. Space Sci.*, *53*, 1401–1418, doi:10.1016/j.pss.2005.07.010.

Withers, P., et al. (2011), Observations of thermal tides in the middle atmosphere of Mars by the SPICAM instrument, *J. Geophys. Res.*, *116*, E11005, doi:10.1029/2011JE003847.

Withers, P., K. Fallows, and M. Matta (2014), Predictions of electron temperatures in the Mars ionosphere and their effects on electron densities, *Geophys. Res. Lett.*, *41*, 2681–2686, doi:10.1002/2014GL059683.